Augmented Reality and Robotic-Assistance for Percutaneous Nephrolithotomy

Federica Ferraguti[1], Marco Minelli[1], Saverio Farsoni[2], Stefano Bazzani[1], Marcello Bonfè[2]
Alexandre Vandanjon[4], Stefano Puliatti[3], Giampaolo Bianchi[3] and Cristian Secchi[1]

Abstract— Percutaneous nephrolithotomy (PCNL) is considered the gold standard for the treatment of patients with renal stones larger than 20 mm in diameter. The success and treatment outcomes of the surgery are very well known to be highly dependent on the precision and accuracy of the puncture step, since it must allow to reach the stone with a precise and direct path. Thus, performing the renal access during PCNL is the most crucial and challenging step of the procedure with the steepest learning curve. In this paper, we propose an innovative solution, based on an AR application combined with a robotic system, that can assist both an expert surgeon in improving the performance of the surgical operation and a novel surgeon in strongly reducing his/her learning curve. The proposed system is validated on a setup including a KUKA LWR 4+ robot and the Microsoft HoloLens as augmented reality headset, through experiments performed by a sample of 11 users.

I. INTRODUCTION

According to the European and the American Urological Associations, percutaneous nephrolithotomy (PCNL) is considered the gold standard for the treatment of patients with renal stones larger than 20 mm in diameter [1]. Its popularity and acceptance among urologists and patients is due to the fact that it is minimally invasive and is associated with low morbidity [2]. The procedure consists of inserting a specific tool (the nephroscope) into the kidney through a percutaneous track created in the patient's lower flank or abdomen. Using fluoroscopy and ultrasonic imagery the urologist inserts a hollow needle into one of the renal calyxes of the kidney. This passage is then dilated, and a percutaneous sheath is inserted to accommodate the nephroscope. The success and treatment outcomes of the surgery are very well known to be highly dependent on the precision and accuracy of the puncture step, since it must allow to reach the stone with a precise and direct path [3]. Thus, performing the renal access during PCNL is the most crucial and challenging step of the procedure with the steepest learning curve. Indeed, it has been shown that a fellow in endourology, with no previous experience in performing PCNL, requires 45 and 105 operations to achieve competence and excellence, respectively, in performing the procedure [4]. One reason why it is challenging for urologists to achieve good proficiency

is that not all training programs during the residency have faculty who perform this procedure. Indeed, in 2011 fewer than half (47%) of graduating U.S. chief residents indicated that PCNL access was routinely obtained by urologists at their institution and this limits the opportunity to pick up the required skills in practice. A 2014 review of case logs from certifying and recertifying urologists found that only 6% performed more than 10 PCNLs during the prior 6 months and urologist-obtained access only occurred in 20% of these cases, while in the other cases the renal access was performed by the radiologist [5].

Urologists have introduced various simulation models to help trainees achieve competency level in a shorter length of time. Simulators used for assessment of PCNL skills include human cadavers, animal tissues [6] and Virtual Reality (VR) simulators to simulate human patients [7] [8]. A recent review on the current training method has been presented in [9], before introducing The Marion K181 PCNL VR simulator. Virtual reality based simulators have been shown to improve the performance of the trainee but they often lack realistic haptic feedback, which is key in improving the skills of the trainee [10]. On the other side, the availability of preoperative information (Computed Tomography (CT) or Magnetic Resonance Imaging (MRI)) of the anatomical parts has been exploited for implementing Augmented Reality (AR) solutions for augmenting the capabilities of the surgeon during the procedure. In particular, in [11] and [12] AR systems are used to support the percutaneous access in percutaneous nephrolithotomy by overlaying a 3D model onto the image from a tablet camera. In [13] the challenge of obtaining an appropriate access to the renal stones in the case of complex anatomical or pathological conditions is addressed. A 3D model generated from MRI is used for trajectory planning and intra-operative augmentation of real-time intraoperative ultrasonography. A recent review on augmented reality systems in surgery is presented in [14]. For experienced surgeons, augmented reality visualization of renal anatomy has been proved to be sufficient to estimate correct needle angles to reach the target. However, several doubts persist whether urologists in training still need additional technical assistance apart from AR support [11].

A different solution for precise percutaneous access in PCNL is represented by robotic assisted systems. PAKY (Percutaneous Access to the Kidney) is a robotic system developed for PCNL to accurately position and insert a needle percutaneously into the kidney [15]. Lately, several works have been presented concerning the development of

[1]Dipartimento di Scienze e Metodi dell'Ingegneria, Università di Modena e Reggio Emilia, Italy. Corresponding author e-mail: federica.ferraguti@unimore.it

[2]Dipartimento di Ingegneria, Università di Ferrara, Italy.

[3]Dipartimento Chirurgico, Medico, Odontoiatrico e di Scienze Morfologiche con interesse Trapiantologico, Oncologico e di Medicina Rigenerativa, Università di Modena e Reggio Emilia, Italy.

[4]Icam - Institut Catholique d'Arts et Métiers, France.

US-guided robotic systems [16]. The common approach consists of a surgical needle attached to a robotic arm that is driven, automatically or teleoperated by the surgeon, in a 3D or 2D imaging volume [3]. More recently, in [17], a collaborative robotic assisted system is proposed to help the surgeon correctly locating the ultrasound probe during the intervention, while the respiratory motion of the patient is compensated. Once the probe is located, the needle insertion is performed. However, if the robot perform some operations autonomously or in teleoperation, the resident or the novel surgeon would not be able to learn how to perform the surgical intervention manually and therefore the goal of providing a system to reduce their learning curve would fail. In the proposed paper, the robot provides just an assistance, without performing any operation in autonomy or in teleoperation. Augmented reality and robotic systems have been combined in different works for performing a precise needle insertion in radiofrequency ablation [18], [19] and in ultrasound-guided biopsy [20]. However, in these papers the robotic system is used to perform autonomously some parts of the operation (i.e. the needle insertion). In the PCNL procedure, executing the puncture step to perform the renal access is the most crucial and challenging step, with the steepest learning curve. If these actions are performed autonomously by the robot, residents or novel surgeons would not learn how to manually perform the complete procedure, especially in its most critical parts.

In this paper, we blend the potentialities of AR support with the technical assistance that can be provided through robotic systems. In particular, we present an innovative solution, based on an AR application combined with a robotic system, that can assist: (i) an expert surgeon in improving the performance of the surgical intervention, by augmenting his/her capabilities (ii) a novel surgeon in strongly reducing his/her learning curve, since the system can provide assistance during the most critical phases of the intervention, especially at the early end of the learning curve when mistakes are certainly more likely. The proposed system will allow to plan the surgical intervention in a pre-operative phase and to assist the surgeon in the intra-operative phase. In particular, the surgeon, wearing an AR headset, will directly see on the body of the patient a reconstructed 3D model of the anatomical parts of interest and the planned trajectory to be followed. Then, he/she will manually guide a robot that holds the nephroscope and will be assisted by feeling virtual forces (*virtual fixtures* [21]) that will keep him/her on the right renal access. The proposed system is validated on a robotic setup and with 11 users performing a task that emulates the renal access in PCNL.

II. PROPOSED SYSTEM ARCHITECTURE

The proposed system architecture, summarized in Fig. 1, consists of an AR application to provide the surgeon with interactive 3D visualizations in all the phases of the operation and a robotic system to assist and guide the surgeon towards the optimal execution of the intervention. In particular, for each surgical operation, we distinguish two different phases:

a *pre-operative phase*, where the 3D model that will be used for the visualization is built and the pre-operative planning of the desired trajectory is performed, and an *intra-operative phase*, where the surgeon performs the surgical intervention by wearing the AR device and with the assistance of the robotic system.

A. Pre-operative phase

The planning of a surgical intervention is typically done on the basis of pre-operative images acquired as CT or MRI of the interested area. Starting from the CT of the area (Fig. 1(a)), we reconstructed the 3D model of the interested area and the organs that are involved in the procedure, both as target or forbidden regions, namely anatomical parts that need to be avoided during the puncturing. The same approach could be easily adopted if the input is MRI. Since in the proposed paper we address the PCNL procedure, we reconstructed the 3D model of: skin, ribs, kidney, calices, stones, ureter, aorta, inferior vena cava and all the neighboring structures (Fig. 1(b)). The 3D reconstruction is performed starting from the DICOM images of the CT/MRI and segmenting the different parts on the basis of their Hounsfield Unit, which is the unit to measure the radiodensity into a CT/MRI. Then, on the basis of the 3D reconstruction, we generated and showed to the surgeon a trajectory that reaches the target (i.e. the renal calix or the kidney stone) while avoiding the forbidden regions (green trajectory in Fig. 1(c)). The surgeon can validate the trajectory or modify it simply by moving the inserted point: the trajectory will update accordingly. Since the system will require reference points to perform a real-time localization of the 3D model on the body of the patient, we applied three electrocardiogram (ECG) electrode patches following a L-shape directly on the back of the patient before the execution of the initial CT scan. In the 3D reconstruction phase the contours of the ECG electrode patches are segmented and included into the 3D model and can be used as markers for the real-time registration, assuming that the conditions of the patient do not change between the pre-operative and the intra-operative phase (i.e. the posture of the patient is face-down, as during the CT scan, and the patches do not move, see Section II-B.1).

B. Intra-operative phase

Once the pre-operative planning of the intervention is concluded, the 3D reconstruction is saved, and it will be used into an Augmented Reality (AR) application developed for an AR headset for visualizing the reconstruction directly on the body of the patient. Since the CT/MRI scan is performed few days before the effective execution of the surgical intervention, a real-time registration is required to intra-operatively align the reconstructed model in the right position and orientation on the body of the patient. The real-time registration is performed on the basis of the three ECG electrode patches (Fig. 1(d)). Details on the registration process will be provided in Section II-B.1. The surgeon, wearing the augmented reality headset (e.g. Microsoft HoloLens), will directly visualize the reconstructed model that, thanks
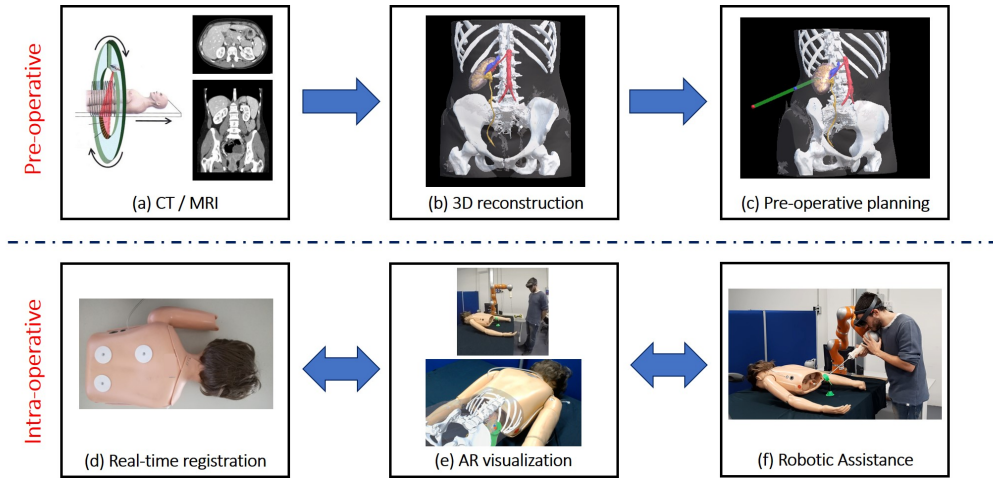
Fig. 1: Conceptual scheme of the proposed architecture.

to the previous registration, will be correctly located on the body of the patient (Fig. 1(e)). Since the insertion trajectory is computed on the basis of the pre-operative CT/MRI scan, it may happen that the trajectory needs to be adjusted depending on the real location of the organs in the intra-operative phase. Thus, thanks to the AR application, the surgeon can directly adjust the insertion point in order to obtain a collision-free trajectory (i.e. a trajectory that still reaches the target while avoiding neighboring organs or ribs).

Once the optimal trajectory has been defined, the surgeon manually guides the robot from an initial position towards the desired trajectory for the percutaneous access. The robot is then used to gently assist the surgeon towards the trajectory. To this aim, we included the generation of virtual fixtures in the robot control scheme (Fig. 1(f)). Virtual fixtures are typically used in haptics and teleoperation architectures and they are generally defined as assistive forces applied to the haptic device that is used as the teleoperation master [21]. These virtual fixtures can be designed to restrict the motion of the master to desired subspaces or volumes in its operational space, or to guide the user towards a desired target, that can be either a specific operating point or a more complex geometric path. In our control architecture, the surgeon manually guides the robot through its end-effector. However, we can still apply the concept of virtual fixtures in order to generate virtual forces on the robot end-effector that can guide the needle (attached at the robot end-effector but handled by the surgeon's hand) towards the desired trajectory. Since the proposed system have to assist a novel surgeon in reducing his/her learning curve, virtual fixtures are designed to intervene only when the surgeon is near to the desired trajectory, and thus for the final refinement of the position and the orientation of the needle. The reason behind this choice is to have the surgeon trying to gain the right percutaneous access by himself/herself and performing the surgical intervention in autonomy but with the assistance of the proposed system that guarantees that the surgical operation is performed successfully without complications,

especially at the early end of the learning curve. Once the surgeon has moved the needle in the right position for the percutaneous access, with the right orientation, then he/she can perform the insertion. The surgeon is assisted by the virtual fixtures even during the needle insertion, in order to keep the needle along the right trajectory towards the target, while avoiding other anatomical structures. In the remaining part of this section we will provide the details on the three technical parts of the system: the real-time registration, the application for AR visualization and the generation of assistive virtual fixtures.

1) Real-time registration: The reconstruction and the segmentation of the 3D patient model allow to define the reference system of the model itself on the basis of the L-shaped positioned triad of ECG electrode patches (Fig. 1(d)). Indeed, the point corresponding to the center of the first patch is used to identify the origin of such reference system, while the line connecting the centers of the first and second patches determines the x-axis unit vector. Finally, the centers of the three patches define the xy-plane. Therefore, the origin and xyz-axis unit vectors of the 3D model reference system can be computed as follows:

$$
\begin{aligned}
\mathbf{O}_b &= \mathbf{P}_0 \\
\mathbf{v}_{b,x} &= \frac{(\mathbf{P}_1-\mathbf{P}_0)}{||(\mathbf{P}_1-\mathbf{P}_0)||} \\
\mathbf{v}_{b,z} &= \mathbf{v}_{b,x} \times \frac{(\mathbf{P}_2-\mathbf{P}_0)}{||(\mathbf{P}_2-\mathbf{P}_0)||} \\
\mathbf{v}_{b,y} &= \mathbf{v}_{b,z} \times \mathbf{v}_{b,x}
\end{aligned}
\tag{1}
$$

where $\mathbf{P}_0, \mathbf{P}_1, \mathbf{P}_2 \in \mathbb{R}^3$ are the position of the centers of the patches, $\mathbf{O}_b \in \mathbb{R}^3$ and $\mathbf{v}_{b,x}, \mathbf{v}_{b,y}, \mathbf{v}_{b,z} \in \mathbb{R}^3$ (as column-vectors) are the origin and the unit vectors of the 3D model reference system. The symbol $\times$ indicates the cross product. Once the 3D model reference system has been defined, the pose of each segmented anatomical part and the desired insertion trajectory, represented by an insertion point on the skin $\mathbf{P}_I \in \mathbb{R}^3$ and a target point on the kidney stone $\mathbf{P}_T \in \mathbb{R}^3$, can be mapped into to such a coordinate system (i.e. $^b\mathbf{P}_I, {}^b\mathbf{P}_T$, where the left apex indicates the reference system). It is worth noting that the position of the

The real-time alignment of the reconstructed 3D model on the body of the patient is performed by localizing the three patches in the current spatial map of the environment, elaborated by the AR device. In particular, we placed one Aruco marker [22] on each patch, so that the centers of the patches coincide with the centers of the markers. By accessing the data coming from the stereo cameras available on the AR headset, we could recognize the unique id-code of the Aruco markers and thus we could determine the position of the pixels that contain the corners of the detected markers. Assuming the knowledge of intrinsic and extrinsic camera parameters, each marker corner detected in the left camera frame can be triangulated with the same corner detected in the right camera frame, so that their 3D coordinates in the headset world reference system can be estimated. To improve the stability of the registration, a moving average filter on a window of 30 samples has been introduced on the spatial coordinates of all the marker corners detected by the AR device. Then, the center of gravity (COG) of the four corners of each marker is kept to determine the central point of the three patches. Therefore, (1) can be used to compute the transformation matrix ${}^{w}\mathbf{T}_{b}$ of the patient body in the world reference system of the AR device:

$$ {}^{w}\mathbf{T}_{b} = \begin{bmatrix} \mathbf{v}_{b,x} & \mathbf{v}_{b,y} & \mathbf{v}_{b,z} & \mathbf{O}_{b} \\ 0 & 0 & 0 & 1 \end{bmatrix} \quad (2) $$

Once the pose of the patient body has been reconstructed, a further transformation has to be computed to express such pose in the robot coordinate system. For this purpose, a registration box (shown in the top-left of Fig. 2) has been prepared, consisting in an open cube in which the three orthogonal internal faces contains an Aruco marker. The box has to be fixed at a known pose with respect to the robot kinematics reference system and its faces have to be detected by the AR device, so that a common reference system can be finally determined. Indeed, we detected and triangulated the corners of each marker and the COG of the first marker corners can be considered as the origin $\mathbf{O}_{c}$ of the cube reference system. Moreover, in this case, being the markers orthogonal to each other, each axis of the cube reference system (with unit vectors $\mathbf{v}_{c,x}, \mathbf{v}_{c,y}, \mathbf{v}_{c,z}$) can be estimated as the normal to the plane that best fits a set of marker corners [23]. Therefore, the transformation matrix ${}^{w}\mathbf{T}_{c}$ from the registration cube to the headset world reference system can be computed as:

$$ {}^{w}\mathbf{T}_{c} = \begin{bmatrix} \mathbf{v}_{c,x} & \mathbf{v}_{c,y} & \mathbf{v}_{c,z} & \mathbf{O}_{c} \\ 0 & 0 & 0 & 1 \end{bmatrix} \quad (3) $$

Figure 2 shows the AR headset world, the patient body and the cube reference systems.

Moreover, assuming the knowledge of ${}^{r}\mathbf{T}_{c}$, i.e. the matrix representing the transformation from the robot to the cube
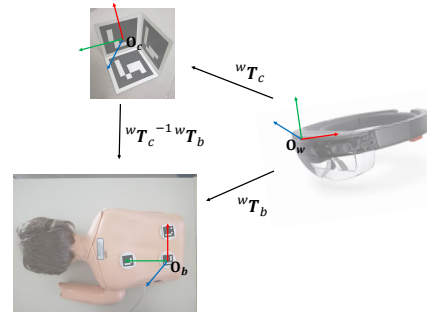

Fig. 2: The reference systems and the transformation matrices among them. The x-axis is depicted in red, the y-axis in blue and the z-axis in green.

Procedure Registration

Data: Input data $({}^{b}\mathbf{P}_{T}, {}^{b}\mathbf{P}_{I}, {}^{r}\mathbf{T}_{c})$
1 Detect markers in the AR device left and right camera frames and estimate their 3D position
2 Apply a moving average filter on the marker corners position
3 When all the cube markers are detected, compute ${}^{w}\mathbf{T}_{c}$
4 When all the markers placed on the patches are detected, compute their COG and ${}^{w}\mathbf{T}_{b}$ from (2)
5 Compute ${}^{r}\mathbf{P}_{T}, {}^{r}\mathbf{P}_{I}$ from (4)

---

reference system, the insertion point and the target point can be transformed to the robot kinematics coordinates (${}^{r}\mathbf{P}_{I}$, ${}^{r}\mathbf{P}_{T}$) as follows:

$$ \begin{aligned} {}^{r}\mathbf{P}_{I} &= {}^{r}\mathbf{T}_{c} \cdot {}^{w}\mathbf{T}_{c}^{-1} \cdot {}^{w}\mathbf{T}_{b} \cdot {}^{b}\mathbf{P}_{I} \\ {}^{r}\mathbf{P}_{T} &= {}^{r}\mathbf{T}_{c} \cdot {}^{w}\mathbf{T}_{c}^{-1} \cdot {}^{w}\mathbf{T}_{b} \cdot {}^{b}\mathbf{P}_{T} \end{aligned} \quad (4) $$

Finally, the whole computational process of the AR device is summarized by Procedure Registration.

2) Augmented reality visualization: The visualization of the AR scene is performed on the basis of the real-time detection of the Aruco markers and the resulting registration matrix ${}^{w}\mathbf{T}_{b}$. Indeed, as depicted in Fig. 1(e), the hologram of the segmented 3D models representing the anatomical parts (ribs and organs) can be rendered overlapping the patient body. Moreover, the hologram of the insertion trajectory can be visualized in order to assist the surgeon in obtaining the right renal access.

3) Assistive virtual fixtures: The goal of the virtual fixtures is to assist the surgeon during the alignment and the insertion of the needle towards the desired trajectory for the right percutaneous access. In order to correctly perform the insertion of the needle, the instrument needs to be first aligned along the insertion direction and with a configuration such that it lies between the patient and the robot, outside the body. Once the instrument is aligned, the insertion can be executed.

Let us consider the insertion point on the skin ${}^{r}\mathbf{P}_{I}$ and the target point on the kidney stone ${}^{r}\mathbf{P}_{T}$ defined in Section II-B.1, with respect to the robot base. The two points are computed in the pre-operative phase according to the 3D reconstruction and lie along the desired trajectory, selected as the one allowing to reach the kidney stone while avoiding
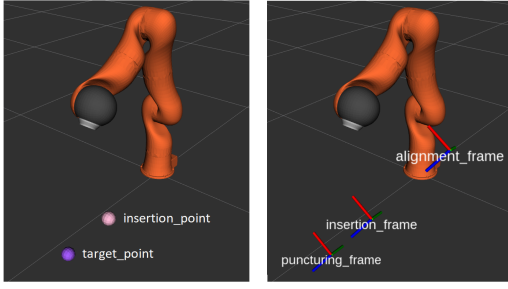
Fig. 3: Left: target point on the kidney stone (purple sphere) and insertion point on the skin (pink sphere) that are computed from the 3D reconstruction. Right: Cartesian frames used for computing the virtual fixtures. The x-axis is depicted in red, the y-axis in blue and the z-axis in green.

other anatomical structures such as, e.g., the ribs. Consider now the insertion plane π, defined as the plane that passes through the insertion point $\mathbf{P}_I$ and that is normal to the insertion direction $\mathbf{P}_T - \mathbf{P}_I$:

$$\pi : \mathbf{a}x + \mathbf{b}y + \mathbf{c}z + \mathbf{d} = 0 \qquad (5)$$

where the parameters $\mathbf{a}, \mathbf{b}$ and $\mathbf{c}$ are the components of the insertion direction unit vector, while $\mathbf{d}$ can be easily computed by substituting the components of the insertion point $\mathbf{P}_I$ into the plane equation (5).

Considering the plane π, as defined in (5) and the insertion direction $\mathbf{P}_T - \mathbf{P}_I$ we can compute the insertion frame $^r\mathbf{T}_I$, i.e. the pose the instrument should have when the needle starts perforating the skin, where r is the robot base reference frame and I is the insertion point, as follows: 1) the z-axis is given by the insertion direction unit vector, 2) the x-axis can be computed considering the unit vector pointing to an arbitrary point on the insertion plane and, 3) the y-axis can be computed as the cross product of the z-axis and the x-axis. Once computed the insertion frame $^r\mathbf{T}_I$, we can calculate the target frame $^r\mathbf{T}_T$ and the alignment frame $^r\mathbf{T}_A$. The target frame of the puncturing $^r\mathbf{T}_T$ represents the pose of the kidney stone, and it can be computed exploiting the distance between the target point $\mathbf{P}_T$ and the insertion point $\mathbf{P}_I$. The alignment frame $^r\mathbf{T}_A$ represents the desired instrument pose at the beginning of the insertion. This frame is computed applying a safety distance d_s to the insertion frame $^r\mathbf{T}_I$ and it is computed such that it lies between the patient and the robot, outside the body. Figure 3 shows an example of computation of the three main frames starting from the target point $\mathbf{P}_T$ and the insertion point $\mathbf{P}_I$. The procedure ComputeRobotFrames summarizes the processing steps that allow to obtain the frames $^r\mathbf{T}_T, ^r\mathbf{T}_I, ^r\mathbf{T}_A$.

In order to generate the virtual fixtures, we divided the execution of the percutaneous renal access for PCNL into three different steps:

- *Alignment*: the robot is in the initial configuration and guides the surgeon towards the alignment frame $^r\mathbf{T}_A$.
- *Stiffening*: the alignment frame $^r\mathbf{T}_A$ is reached; the robot have to change its stiffness in order to allow

---

Procedure ComputeRobotFrames

Data: Input data $(^r\mathbf{P}_T, ^r\mathbf{P}_I, ^r\mathbf{T}_c)$
1 Compute the parameters $\mathbf{a}, \mathbf{b}, \mathbf{c}, \mathbf{d}$ of the insertion plane π from (5)
2 Fix the orientation of the frames considering the z-axis normal to π
3 Set the insertion frame $^r\mathbf{T}_I$
4 Set the target frame on kidney stone $^r\mathbf{T}_T$
5 Set the alignment frame $^r\mathbf{T}_A$ applying the safety distance d_s

---

the surgeon to move the instrument along the insertion direction and not outside the desired trajectory.
- *Guidance*: the desired stiffness is reached. The surgeon can now move the instrument along the insertion direction to perform the needle insertion.

The virtual fixtures are computed in all the three steps as:

$$\mathbf{F_e} = \mathbf{k_F}\Delta\mathbf{x_e} - \mathbf{b_F}\dot{\mathbf{x}}_\mathbf{e} \qquad \boldsymbol{\tau}_r = \mathbf{k_T}\Delta\theta_\mathbf{b} - \mathbf{b_T}\dot{\theta}_\mathbf{b} \qquad (6)$$

where $\mathbf{F_e} \in \mathbb{R}^3$ are the commanded forces with respect to the robot end-effector, $\mathbf{k_F}, \mathbf{b_F} \in \mathbb{R}^3$ are linear spring-damper coefficients, $\Delta\mathbf{x_e} \in \mathbb{R}^3$ are the position errors between the desired frame and the robot frame with respect to robot end-effector and $\dot{\mathbf{x}}_\mathbf{e} \in \mathbb{R}^3$ are the linear velocities of the robot end-effector with respect to robot end-effector. $\boldsymbol{\tau}_r \in \mathbb{R}^3$ are the commanded torques with respect to the robot base, $\mathbf{k_T}, \mathbf{b_T} \in \mathbb{R}^3$ are rotational spring-damper coefficients, $\Delta\theta_\mathbf{b} \in \mathbb{R}^3$ are the rotational errors between the desired frame and the robot frame with respect to the robot base and $\dot{\theta}_\mathbf{b} \in \mathbb{R}^3$ are the angular velocities of the robot end-effector with respect to the robot base.

During the alignment step, the desired frame is imposed to be the alignment frame $^r\mathbf{T}_A$. In this step, if the initial configuration of the robot is far from the alignment frame, the position errors $\Delta\mathbf{x_e}$ and the rotational errors $\Delta\theta_\mathbf{b}$ could be very high. In order to avoid excessive forces and torques, the linear spring coefficients $\mathbf{k_F}$ and rotational spring coefficients $\mathbf{k_T}$ are set as follow:

$$\mathbf{k_F} = \mathbf{k_F^{min}} + \left(1 - e^{\frac{\|\Delta\mathbf{x_e}\|}{\tau_F}}\right)\left(\mathbf{k_F^{max}} - \mathbf{k_F^{min}}\right)$$
$$\mathbf{k_T} = \mathbf{k_T^{min}} + \left(1 - e^{\frac{\|\Delta\theta_\mathbf{b}\|}{\tau_T}}\right)\left(\mathbf{k_T^{max}} - \mathbf{k_T^{min}}\right) \qquad (7)$$

where $\mathbf{k_F^{min}}, \mathbf{k_F^{max}}, \mathbf{k_T^{min}}, \mathbf{k_T^{max}}$ are the minimum and the maximum value of the linear spring coefficients and the rotational spring coefficients, respectively, and τ_F, τ_T are user-defined parameter used to define the transition of the coefficient between the limit values. The idea is that for high errors the forces and the torques should be low, in order to allow the surgeon to freely move the robot. As the error decrease the surgeon is increasingly being attracted to the desired configuration. Thanks to this solution, virtual fixtures intervene only when the surgeon is near to the desired trajectory, and thus for the final refinement of the position and the orientation of the needle. The surgeon can try to gain the right percutaneous access by himself/herself in autonomy but the assistance of the proposed system guarantees that the surgical operation is performed successfully without complications. Once the alignment frame is reached, the robot changes its stiffness to a desired value $\mathbf{k_F^g}, \mathbf{k_T^g}$ in a desired

time t_s. This stiffening allows the robot to increase the accuracy with which the insertion trajectory is followed and allows the surgeon to start the assisted insertion of the needle. In particular, the stiffness will be low along the trajectory direction, while it will be high in the other components, in order to prevent the user from exiting the desired trajectory. In the guidance state the desired frame is set to be the target frame ${}^r\mathbf{T}_T$ and the spring coefficients are kept constant to the values of the stiffening step $\mathbf{k_F^g}, \mathbf{k_T^g}$. In order to allow the surgeon to move the instrument along the insertion trajectory, the value of the linear spring coefficient along the z-axis is set equal to 0. In this way, in the guidance step, the surgeon can rely on the kinesthetic feedback arising from tool/tissue contact to properly navigate the tool, since this is the only reacting force felt along the insertion direction.

III. EXPERIMENTAL VALIDATION

The experimental validation is described in the following and it is organized into three main activities:

- *Registration*: the accuracy of the location of the 3D reconstruction of the anatomical model of the patient with respect to the real body is evaluated.
- *Performances*: a comparison between the performances of the system with and without the use of the virtual fixtures is reported.
- *Usability*: a validation on a sample of 11 users is performed and a statistical analysis of the usability of the system is reported.

The experimental setup included a KUKA LWR 4+ 7-DOF robot able to return the virtual fixtures to the user. The surgical scenario is reproduced using a 3D printed handle with a needle, mounted on the end-effector of the robot. The AR headset being used are the Microsoft HoloLens that are worn by the user to display the 3D reconstruction of the body of the patient and to perform the real-time registration. The 3D reconstruction is visualized on a manikin lying down on the table where the robot is fixed. Once the registration is accomplished, the user is free to handle the surgical tool and perform the procedure, following the steps described in section II-B.3: *alignment*, *stiffening* and *insertion*. In the experiments in which the virtual fixtures are turned off, the procedure is executed manually, with the robot gravity-compensated and using as feedback the only visual information provided by the HoloLens. We will hereafter refer to these experiments as *manual experiments*. In the experiments in which the virtual fixtures are turned on, the user still has the visual information but the movements are assisted by the virtual fixtures generated through the robot, following the description reported in II-B.3. We will hereafter refer to these experiments as *assisted experiments*. In the *manual experiments* the *stiffening* step is skipped. The experiments have been performed by a total of 11 users (4 female, 7 male, from 24 to 32 years old), Each user was asked to perform both the *manual experiment* and the *assisted experiment*. Moreover, the users were asked to fill in a questionnaire, in order to obtain a qualitative evaluation of

the user's perspective. The accompanying video clip shows the experiment performed by one of the users.

A. Registration

In order to evaluate the quality of the registration, we compared the transformation matrix ${}^r\mathbf{T}_b$ of the patient body in the robot reference system that is provided by the HoloLens with the one computed executing the same registration algorithm but starting from the position of the centers of the patches measured using the robot. To capture this information we acquired the robot position after physically moving the robot to the patches. The translation and orientation error norm between the two trasformation matrices resulted to be 15.80 mm and 4.12 deg, respectively. The orientation error is computed as the absolute value of angle in the axis-angle representation of the rotation matrix ${}^r\mathbf{R}_b(h)^T \ {}^r\mathbf{R}_b(r)$, where ${}^r\mathbf{R}_b(h)$ is the transformation matrix of the patient body in the robot reference system provided by the HoloLens while ${}^r\mathbf{R}_b(r)$ is the transformation matrix of the patient body in the robot reference system computed using the robot. The resulting orientation error is quite contained while the translation error is more relevant. This is due to the fact that the orientation estimation is mediated by the use of all the markers, while the translation strongly depends on the ability of the HoloLens camera to recognize the position of the single marker. As will be described in Section IV, this error can be strongly mitigated by considering additional information, such as merging the HoloLens data with the information acquired in real-time through an ultrasound probe or through an external tracking system, or by integrating into the architecture an automatic CT-ultrasound registration as proposed in [24], in order to achieve an acceptable error lower than 4-5 mm, which is almost the half of the average size of the calyx diameter. Moreover, in a real PCNL procedure, the registration can be further improved by compensating the respiratory motion of the patient, as suggested in [17].

B. Performances

The performances of the system are evaluated comparing the results of the *manual experiments* and the ones from the *assisted experiments*. Figure 4 reports the evolution over time of the translation and the orientation error norm between the desired position of the instrument and its real position. The plots refer to the experiments of one random user. The orientation error norm is computed considering the angle between the desired direction and the real one, and it can be calculated as:

$$\|\arccos(\bar{\mathbf{z}}_{\mathbf{m}} \cdot \bar{\mathbf{z}}_{\mathbf{d}})\| \tag{8}$$

where $\bar{\mathbf{z}}_{\mathbf{m}}$ and $\bar{\mathbf{z}}_{\mathbf{d}}$ denotes the measured and the desired z-axis unit vector of the robot end-effector, which desirably coincides with the insertion direction. The symbol $\cdot$ it is used to indicate the dot product. In (8) we do not consider the other components, since a rotation around the z-axis does not influence the performances of the insertion task.

In particular, the plots on the left in Fig. 4 show the values of the errors during the *alignment step*, where the target is the alignment frame $^r\mathbf{T}_A$. The plots on the right report the values of the errors during the *insertion step*, where the target is the target frame $^r\mathbf{T}_T$. The *stiffening step* is omitted since it takes place only for the *assisted experiment*. From the results shown in Fig. 4, we can observe that the execution time for the *assisted experiment* is smaller or, at least, comparable to the execution time of the *manual experiment*. However, it can be observed that the errors for the *assisted experiment* are clearly less than the ones of the *manual experiment*.

Figure 5 reports the trajectory and the forces of/on the instrument during the *assisted experiment*. During the *alignment step* the forces attract the robot towards the alignment position. However, the user can still correct the robot trajectory. This can be seen in the left plot where the forces push to the alignment position but the movement follows another trajectory. This behavior is due to the user, that moves the instrument along a different trajectory to avoid a collision with the patient body. During the *insertion step* the virtual fixtures keep the robot along the insertion direction and do not allow the tip of the instrument to go beyond the target. This behavior can be observed 1) near the target position, where the forces push the instrument to go back and 2) outside the insertion position, where the user intentionally tried to take the robot out of the insertion direction but the fixtures take the instrument on the right trajectory. In order to evaluate the improvements in the performances when the procedure is executed using the virtual fixtures, we decided to conduct a statistical analysis over the following metrics: 1) the execution time, 2) the translation error at the target and 3) the root mean square of the orientation error during the insertion. Table I reports the mean values and the standard deviation values of the described metrics for both the *manual experiments* and the *assisted experiments*. These results confirm what we observed in Fig. 4 and allow us to state the positive contribution of the virtual fixtures when performing the procedure. Moreover, the results collected during the task execution have been evaluated applying a one-way analysis of variance (ANOVA), with the aim of revealing if the influence of robot assistance is relevant (i.e. *p*-value lower than 0.05). The analysis shows that the influence is relevant for the linear and angular accuracy, while it is not for the execution time. The value of the execution time is then influenced by the capabilities of the users.

C. Usability

The effort required to use a system or a device defines its usability. In order to state that the use of the virtual fixtures makes the system more usable with respect to the execution of the procedure with only the AR support, we conducted a statistical analysis over the NASA Task Load Index (NASA-TLX) [25]. The NASA-TLX rates the perceived workload when assessing a task and it is calculated on the basis of a questionnaire which is filled in by the users after having performed the task. The questionnaire is

TABLE I

	Manual		Assisted		*p*-value
	mean	std. d.	mean	std. d.	
Execution time [s]	25.89	14.90	19.56	4.59	0.193
Translation error [mm]	37.93	24.15	15.18	12.75	0.012
Orientation error [deg]	29.75	30.85	1.53	0.54	0.007

Performance results comparing the use of virtual fixtures with respect to the manual execution of the procedure.

TABLE II

	Manual		Assisted		*p*-value
	mean	std. d.	mean	std. d.	
NASA-TLX	55.30	14.04	28.64	14.53	0.0003

NASA Task Load Index results comparing the use of virtual fixtures with respect to the manul execution of the procedure.

based on six questions, each rated from 5 to 100, with 20 increments. We decided to calculate the Raw TLX, which is the mean value of the user rates on the six questions. Table II reports the mean values and the standard deviation values of the NASA-TLX for both the *manual experiments* and the *assisted experiments*. We can observe that both the mean value and the standard deviation of the NASA-TLX for the *assisted experiments* are less than the ones obtained for the *manual experiments*. This allow us to state that the virtual fixtures return a positive contribution in terms of usability of the system and not only from the performance point of view, if compared to the application of a sole AR support. As for the performances, we included in Table II the *p*-value resulting from the ANOVA analysis and it resulted that the task load is influenced by the robot assistance.

IV. CONCLUSIONS AND FUTURE WORKS

In this paper, we proposed an innovative solution, based on an AR application combined with a robotic system,
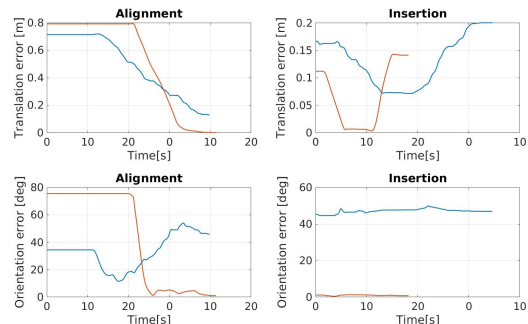

Fig. 4: Translation and orientation error norm between the robot position and the alignment frame during the alignment step (left) and the robot position and the target frame during the guidance step (right). Comparison between *manual experiments* (blue lines) and *assisted experiments* (orange lines).
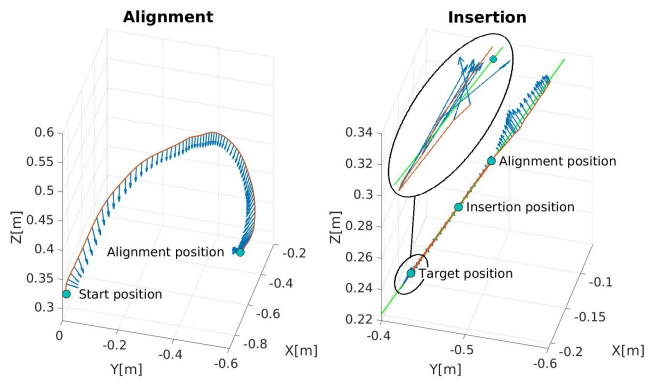
Fig. 5: Robot trajectory (orange line), robot forces (blue arrows) and desired insertion direction (green line) during the alignment step (left) and the guidance step (right).

that can assist both an expert surgeon in improving the performance of the surgical operation and a novel surgeon in strongly reducing his/her learning curve. The paper addressed percutaneous nephrolithotomy (PCNL) as use case, since it is considered to be the gold standard for the treatment of patients with renal stones. However, the proposed system architecture can be easily adopted in all the surgical procedures that require pre-operative planning and intra-operative navigation for gaining access to a specific target, especially in cases where the intervention learning curve for novel surgeons is very steep.

Future works aim at improving the registration procedure by including information acquired in real-time through a 2D or 3D ultrasound probe and by compensating the respiratory motion of the patient. Moreover, we will perform an extensive evaluation with different groups of users, in order to validate the overall system. The idea is to have both residents and expert surgeons performing PCNL on phantoms that emulate the human abdomen. The validation will be performed by dividing the surgeons into different groups with and without the assistance of the proposed system, and by comparing the different performances.

REFERENCES

[1] D. S. Morris, J. T. Wei, D. A. Taub, R. L. Dunn, J. S. Wolf, and B. K. Hollenbeck, "Temporal trends in the use of percutaneous nephrolithotomy," vol. 175, pp. 1731–1736, 2006.

[2] J. de la Rosette, D. Assimos, M. Desai, J. Gutierrez, J. Lingeman, R. Scarpa, and A. Tefekli, "The clinical research office of the endourological society percutaneous nephrolithotomy global study: Indications, complications, and outcomes in 5803 patients," *J. of Endourology*, vol. 25, no. 1, pp. 11–17, 2011.

[3] P. L. Rodrigues, N. F. Rodrigues, J. Fonseca, E. Lima, and J. Vilaca, "Kidney targeting and puncturing during percutaneous nephrolithotomy: recent advances and future perspective," *J. of Endourology*, vol. 27, no. 7, pp. 826–834, 2013.

[4] S. A. Ziaee, M. M. Sichani, A. H. Kashi, and M. Samzadeh, "Evaluation of the learning curve for percutaneous nephrolithotomy," vol. 7, no. 4, pp. 226–231, 2010.

[5] M. Borofsky, M. Rivera, C. Dauw, A. Krambeck, and J. Lingeman, "Electromagnetic guided percutaneous renal access outcomes among surgeons and trainees of different experience levels: A pilot study," *Urology*, 2019.

[6] W. L. Strohmaier and A. Giese, "Ex vivo training model for percutaneous renal surgery," *Urological Research*, vol. 33, pp. 191–193, 2005.

[7] S. Mishra, A. Kurien, R. Patel, P. Patil, A. Ganpule, V. Muthu, R. B. Sabnis, and M. Desai, "Validation of virtual reality simulation for percutaneous renal access training," *J. of Endourology*, vol. 24, no. 4, pp. 635–640, 2010.

[8] A. G. Papatsoris, T. Shaikh, D. Patel, A. Bourdoumis, C. Bach, N. Buchholz, J. Masood, and I. Junaid, "Use of a virtual reality simulator to improve percutaneous renal access skills: A prospective study in urology trainees," *Urologia Internationalis*, vol. 89, pp. 185–190, 2012.

[9] B. Sainsbury, M. Lacki, M. Shahait, M. Goldenberg, A. Baghdadi, L. Cavuoto, J. Ren, M. Green, J. Lee, T. D. Averch, and C. Rossa, "Evaluation of a virtual reality percutaneous nephrolithotomy (pcnl) surgical simulator," *Frontiers in Robotics and AI*, vol. 6, p. 145, 2020.

[10] D. Pinzon, S. Byrns, and B. Zheng, "Prevailing trends in haptic feedback simulation for minimally invasive surgery," *Surgical Innovation*, vol. 23, no. 4, pp. 415–421, 2016.

[11] J. J. Rassweiler, M. Muller, M. Fangerau, J. Klein, A. S. Goezen, P. Pereira, H.-P. Meinzer, and D. Teberd, "ipad-assisted percutaneous access to the kidney using marker-based navigation: Initial clinical experience," *European Urology*, vol. 61, no. 3, pp. 628–631, 2012.

[12] M. Muller, M. C. Rassweiler, J. Klein, A. Seitel, M. Gondan, M. Baumhauer, D. Teber, J. J. Rassweiler, H. P. Meinzer, and L. Maier-Hein, "Mobile augmented reality for computer-assisted percutaneous nephrolithotomy," *Int. J. of Computer Assisted Radiology and Surgery*, vol. 8, pp. 663–675, 2013.

[13] Z.-C. Li, K. Li, H.-L. Zhan, K. Chen, J. Gu, and L. Wang, "Augmenting intraoperative ultrasound with preoperative magnetic resonance planning models for percutaneous renal access," *BioMedical Engineering OnLine*, vol. 11, no. 60, pp. 1–16, 2012.

[14] P. Vavra, J. Roman, P. Zonca, P. Ihnat, M. Nemec, J. Kumar, N. Habib, and A. El-Gendi, "Recent development of augmented reality in surgery: A review," *J. of healthcare engineering*, vol. 2017, 2017.

[15] L.-M. Su, D. Stoianovici, T. Jarrett, A. Patriciu, W. Roberts, J. Cadeddu, S. Ramakumar, S. Solomon, and L. Kavoussi, "Robotic percutaneous access to the kidney: Comparison with standard manual access," *J. of endourology / Endourological Society*, vol. 16, pp. 471–4755, 10 2002.

[16] P. Cinquin, "How today's robots work and perspectives for the future," *J. of visceral surgery*, vol. 148, no. 5S, pp. e12–e18.

[17] H. Li, I. Paranawithana, Z. H. Chau, L. Yang, T. S. K. Lim, S. Foong, F. C. Ng, and U. Tan, "Towards to a robotic assisted system for percutaneous nephrolithotomy," in *IEEE/RSJ Int. Conf. on Intelligent Robots and Systems*, Madrid, Spain, 2018.

[18] R. Wen, W.-L. Tay, B. P. Nguyen, C.-B. Chng, and C.-K. Chui, "Hand gesture guided robot-assisted surgery based on a direct augmented reality interface," *Computer Methods and Programs in Biomedicine*, vol. 116, no. 2, pp. 68–80, 2014.

[19] L. Yang, C.-K. Chui, and S. Chang, "Design and development of an augmented reality robotic system for large tumor ablation," *Int. J. of Virtual Reality*, vol. 8, 12 2015.

[20] C. Freschi, E. Troia, V. Ferrari, G. Megali, A. Pietrabissa, and F. Mosca, "Ultrasound guided robotic biopsy using augmented reality and human-robot cooperative control," in *Annual Int. Conf. of the IEEE Engineering in Medicine and Biology Society*, 2009.

[21] F. Ferraguti, N. Preda, M. Bonfè, and C. Secchi, "Bilateral teleoperation of a dual arms surgical robot with passive virtual fixtures generation," in *IEEE/RSJ Int. Conf. on Intelligent Robots and Systems*, Hamburg, Germany, 2015.

[22] F. J. Romero-Ramirez, R. Muñoz-Salinas, and R. Medina-Carnicer, "Speeded up detection of squared fiducial markers," *Image and vision Computing*, vol. 76, pp. 38–47, 2018.

[23] P. Corke, *Robotics, vision and control: fundamental algorithms in MATLAB® second, completely revised*. Springer, 2017, vol. 118.

[24] W. Wein, O. Kutter, A. Aichert, D. Zikic, A. Kamen, and N. Navab, "Automatic non-linear mapping of pre-procedure CT volumes to 3D ultrasound," in *IEEE Int. Symposium on Biomedical Imaging: From Nano to Macro*, 2010.

[25] S. G. Hart and L. E. Staveland, "Development of nasa-tlx (task load index): Results of empirical and theoretical research," in *Advances in psychology*. Elsevier, 1988, vol. 52, pp. 139–183.